ACS Energy LETTERS
http://pubs.acs.org/journal/aelccp

Correlations between Immobilizing Ions and Suppressing Hysteresis in Perovskite Solar Cells

Yicheng Zhao,[†,‡] Wenke Zhou,[†,‡] Wei Ma,[§] Sheng Meng,[§] Heng Li,[†,‡] Jing Wei,[†,‡] Rui Fu,[†,‡] Kaihui Liu,[†,‡] Dapeng Yu,[†,‡] and Qing Zhao*,[†,‡]

[†]State Key Laboratory for Mesoscopic Physics, School of Physics, Peking University, 100871 Beijing, China
[‡]Collaborative Innovation Center of Quantum Matter, 100084 Beijing, China
[§]Institute of Physics, Chinese Academy of Sciences, 100190 Beijing, China

Supporting Information

ABSTRACT: **Ion migration has been regarded as the major cause of photocurrent hysteresis. Here we use photoluminescence (PL) and optical images, combined with Galvanostatic measurement, to detect the ionic motion. We observe an irreversible PL and optical transmittance change after electric poling. By comparing a neat perovskite film with the sample coated by poly(methyl methacrylate) (PMMA), polyethylene glycol (PEG), and [6,6]-phenyl-C61-butyric acid methyl ester (PCBM), we found that PCBM effectively inhibits ionic motion near the surface of the perovskite.We further evidenced the donor−acceptor complex formed between PCBM and perovskite, implying the mechanism of inhibited ion migration by PCBM. We close by demonstrating that PCBM can also be introduced on the top of perovskite fim in an n−i−p TiO_2 planar structure, to achieve an average 14% steady-state output over 2.3×10^5 s (∼64 h). This work highlights the importance of inhibiting ionic motion in perovskite solar cells.**

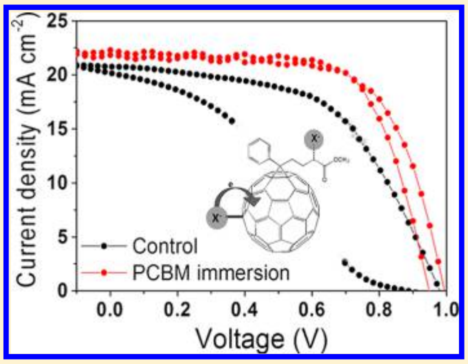

Organometal trihalide perovskites, typically $CH_3NH_3PbI_3$ ($MAPbI_3$), are attractive light-absorber materials in the photovoltaic field, owing to efficient ambipolar transport behavior and large optical absorption.[1−5] Although solution-processed perovskite solar cells (PSCs) have great advantages of low cost and convenient manufacture, there are two obstacles that remain for commercial application, photocurrent hysteresis and performance stability.[6−10] The hysteresis makes it confusing and difficult to evaluate the actual power conversion efficiency (PCE) of PSCs. So far, it is still very challenging to achieve hysteresis-free devices in and n−i−p structure, and the longest holding time at the maximum power point (MPP) was usually reported within a few hundred seconds in the architecture containing TiO_2.[9,11−16] Ion migration has been confirmed in the organometal halide perovskite film and has been considered as a major cause for the observed hysteresis.[17−24] Considering the fact that ionic mobility is very small with a long relaxation time,[19] it can be related to the current hysteresis and other slow processes observed in PSCs.

In this work, we developed an integrated method, Galvanostatic measurement, in situ photoluminescence measurement before and after electric poling, and real time recording of optical microscopic images to characterize ion migration in perovskite films. Moreover, by comparing the perovskite film with many coating layers ([6,6]-phenyl-C61 butyric acid methyl ester (PCBM), poly(methyl methacrylate) (PMMA), and polyethylene glycol (PEG)), we found that PCBM has a special effect on inhibiting ionic motion, and we attributed the hysteresis-free behavior in inverted PSCs to the inhibited ionic motion by PCBM, in addition to the previously mentioned mechanisms.[6,7,31] Further characterizations revealed that PCBM can form astrong bond with undercoordinated atoms at the exposed surface of a perovskite film. After that, we further found that devices with TiO_2 n−i−p structure also present significantly suppressed hysteresis and improved stability (around 64 h stability in MPP tracking) if PCBM chemically absorbed on the exposed surface of perovskite film.

To characterize ion migration in a perovskite film under an applied electric field, a setup is established to realize in situ photoluminescence (PL) characterization with standard Galvanostatic measurement,[19] as is illustrated in Figure 1a. In this setup, the lateral structure (Au/perovskite/Au) was specifically fabricated to realize this in situ characterization,

Received: April 12, 2016
Accepted: June 14, 2016
Published: June 14, 2016

DOI: 10.1021/acsenergylett.6b00060
ACS Energy Lett. 2016, 1, 266−272

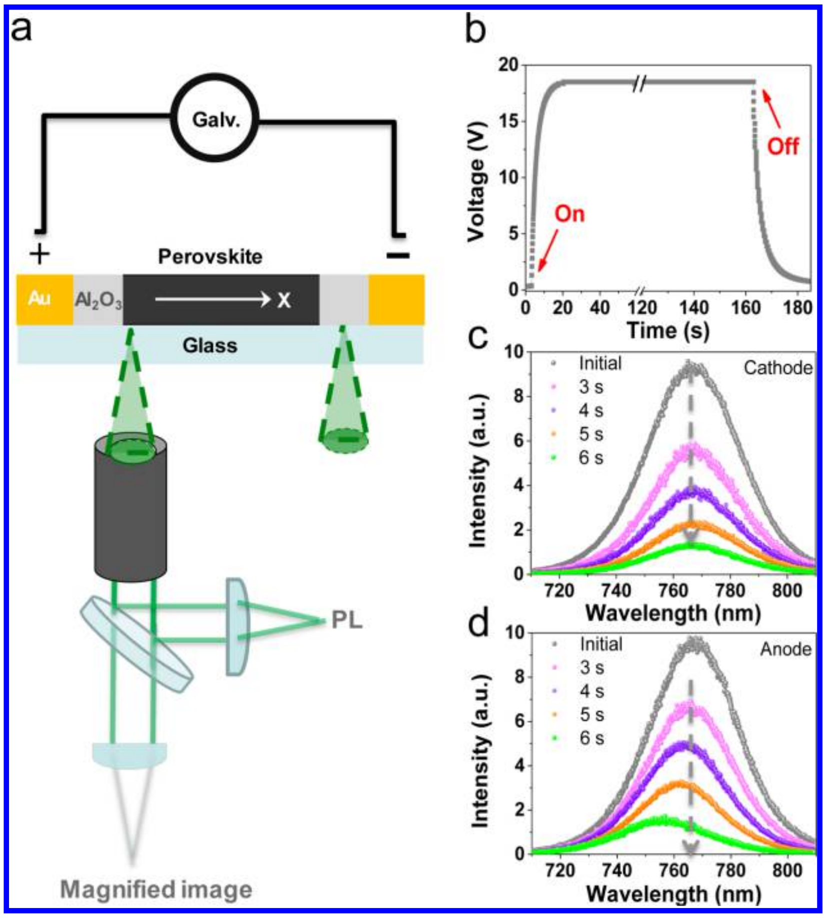

Figure 1. (a) Schematic illustration of the in situ PL characterization with Galvanostatic measurement. The lateral structure consists of planar electrodes composed of a 3 nm Al_2O_3 film and Au (length: 10 mm; width: 0.5 mm; height: 150 nm). The gap of these two electrodes is close to 50 μm. (b) Voltage−time (V−t) curve for a fixed direct current at 10 nA. The on and off indicate the current switches on and off, respectively. (c) PL spectra show a significant decrease at the positive pole (cathode) after electric poling at 1 V/μm for 6 s. (d) PL spectra show a significant decrease at the negative pole (anode) after electric poling at 1 V/μm for 6 s, accompanied by a strong blue shift from ∼765 to 757 nm in the spectra.

and the dynamic process is recorded using both PL spectra and applied voltage. Unless otherwise stated, the measurements are conducted in ambient air. For Galvanostatic measurement, a standard method to characterize ion migration in the ionic conductor is used; upon switching the current from 0 nA to a preset value of 10 nA, the voltage instantaneously reaches ∼1 V and then gradually increases to a larger value of ∼18 V (Figure 1b). During this slow process, both the electron and ion contribute to the conductivity, $j = (\sigma_{\text{ion}} + \sigma_{\text{electron}})E$. As ions gradually accumulate at the two sides, a compositional gradient to block the current gradually forms. This blocking effect demands a larger voltage to retain the constant current (10 nA). At last, the voltage increases to the saturation value where only electronic conductivity exists (Figure 1b). This slow process strongly suggests that ionic transport exists in the film with an extremely small diffusion coefficient of $\sim 10^{-8}$ cm^2 s^{-1}[18,19] compared to that of electronic transport, 10^{-1} cm^2 s^{-1}.[5]

Considering the fact that ion migration will induce excess defects (V_I, I_{MA}) in the film,[21,22] especially at the two sides of a sample, in situ PL characterization is used here to further confirm this process. PL intensity decreases after the voltage switches on at both the anode and cathode by approximately 1 order of magnitude in 6 s (Figure 1c,d), indicating that defect states increase in the perovskite film with time after applying an electric field across the film. In addition, the peak position after electric poling has no visible shift near the cathode pole (Figure 1c), while a large blue shift from 767 to 757 nm is observed near the anode (Figure 1d), which may originate from the strong band-filling effect induced by V_I with n-doping.[25,26] Moreover, an irreversible process for the PL spectra after switching off the current is observed (Figure S1, Supporting Information), as is consistent with the decay process in Figure 1b. This irreversible process implies that a change of PL intensity will be maintained after electric poling, which is consistent with results by Xiao et al.[21,22]

With that in mind, we further move on to use PL mapping in a fixed region of about 30 × 50 μm^2 on a perovskite film before and after 10 s of electric poling (∼0.35 V/μm) along the x direction (Figure 2a,b). The PL intensity in the entire region has a similar value before electric poling (Figure 2a), but it evolves into a quasi-Gaussian distribution after poling (Figure 2b). The PL intensity decreases most significantly at the electrode sides, almost 1/6 of that in the middle position. This distribution resembles an ionic distribution as predicted in macroscopic theory of mixed conduction.[27−29] As is expected below, the largest variation of stoichiometric excess or vacancy of mobile ions is located at the two electrodes, $N = N_0 + A(x/L - 0.5)$,[27] where N_0 is the initial concentration, L is the length of the sample (50 μm), and A is a constant depending on the ionic conductivity of the material. The significantly quenched PL can

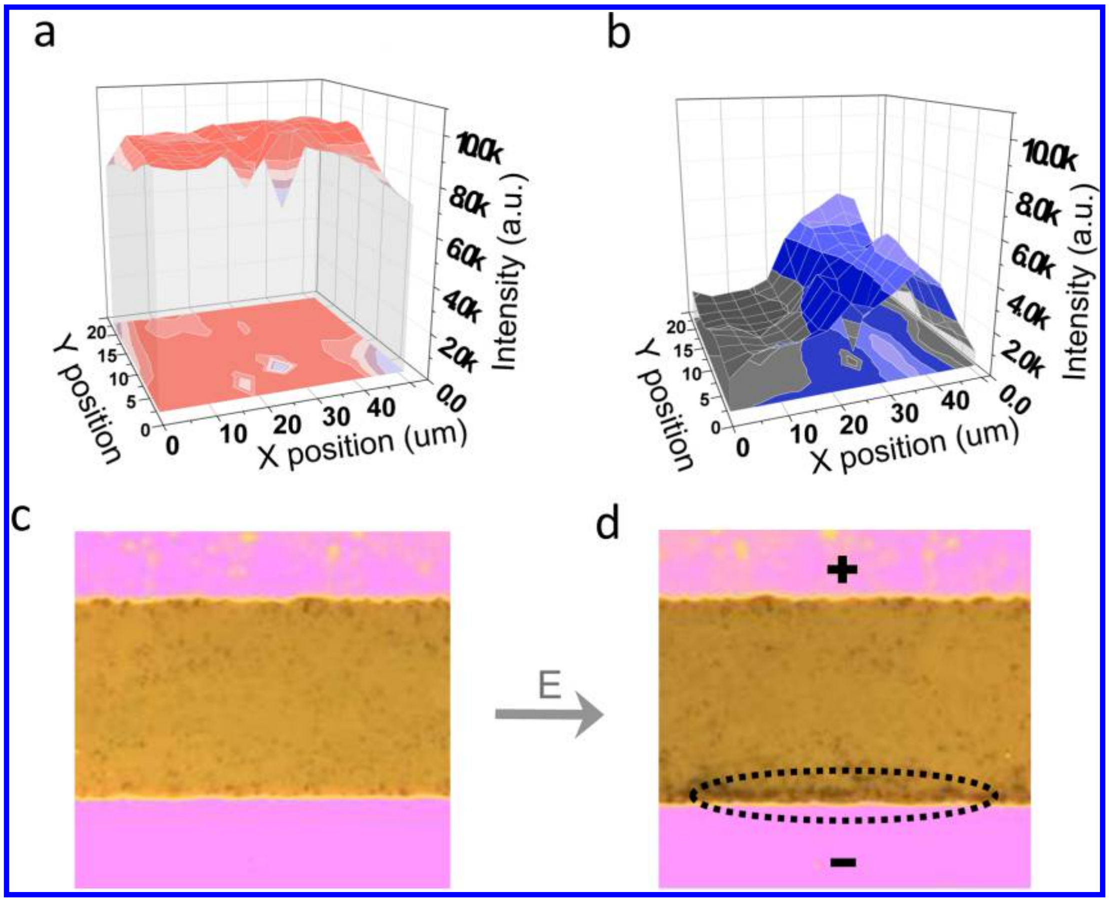

Figure 2. PL mapping tests on a 30 × 50 μm^2 region of perovskite film before (a) and after (b) the aforementioned Galvanostatic measurement with ∼0.35 V/μm. Optical microscopic image of the perovskite film before (c) and after (d) accelerated electric poling at 1 V/μm for 20 s.

be reasonably attributed to the excess defect states induced by ionic motion, where the two sides of the film have the largest amount of defect states (Figure 2b). More than that, PL mapping on the peak position also presents an obvious difference before and after electric poling (Figure S2, Supporting Information), consistent with the results in Figure 1d.

Accelerated ionic motion under a high field of 1 V/μm can cause image contrast change under optical microscopic observation (Figure 2c,d), as schematically shown in the measurement setup in Figure 1a. The contrast change from panel c to d in Figure 2 is possibly due to the composition or morphology change during electric poling of a lateral structure device. The snapshots of this dynamic process (Figure 2d) demonstrate the drift of ions in the film, with more black dots appearing at the anode. These black dots may come from the loss of iodine in the area close to the anode if the I^- ion is the main migration species, although the MA^+ ion was also reported. The finding of ion drift in optical imaging is generally in agreement with previous study by Xiao et al.[21]

The above observations suggest that ion drift under an electric field introduces defect states in the perovskite film. To further support our scenario on the density of defect states induced by ion migration, we use density function theory (DFT) calculation to reveal how these stable defect states are formed when ion migration occurs. Details of DFT calculation are shown in the Supporting Information. The underlying physical picture and simulation results are demonstrated in Figure 3. Iodine-rich and iodine-poor conditions will be realized in different areas of the perovskite film after electric poling, as is shown in Figure 3a,c. Differing from previous calculations in the bulk of the film, in our slab model, deep-level defects will form near the film surface due to I trimers and Pb dimers in Figure 3a−c (∼0.3 eV below the conduction band minimum (CBM)), serving as nonrecombination centers (Figure 3d−f).[30] This result offers powerful evidence of our explanation of the PL quenching behavior observed in Figure 2b.

By using these characterization methods, we further move on to detect the influence of different coating layers on ionic motion in the perovskite. Here, PMMA, PEG, and PCBM are selected to spin-coat on the perovskite film, and lateral devices are fabricated. We observe that optical images and PL spectra show little change during 1 min of poling (1 V/μm) after the three material coatings (Figure S3), compared with the drastic change in the control sample. We also conduct experiments in vacuum and find that optical images present indiscernible change if we put the sample in vacuum system (1 μTorr) under the same poling condition (Figure S3, Supporting Information). These results are consistent with those of T. Leijten et al.[23] that moisture can enhance the ionic motion in perovskites and that any coating layers on the perovskite or in vacuum conditions can relieve the detrimental effect induced by ambient moisture. This irreversible interaction with water under bias is vividly demonstrated, implying the importance to conduct stability tests with strict encapsulation. More than that, for the conductance and Galvanostatic measurements in the

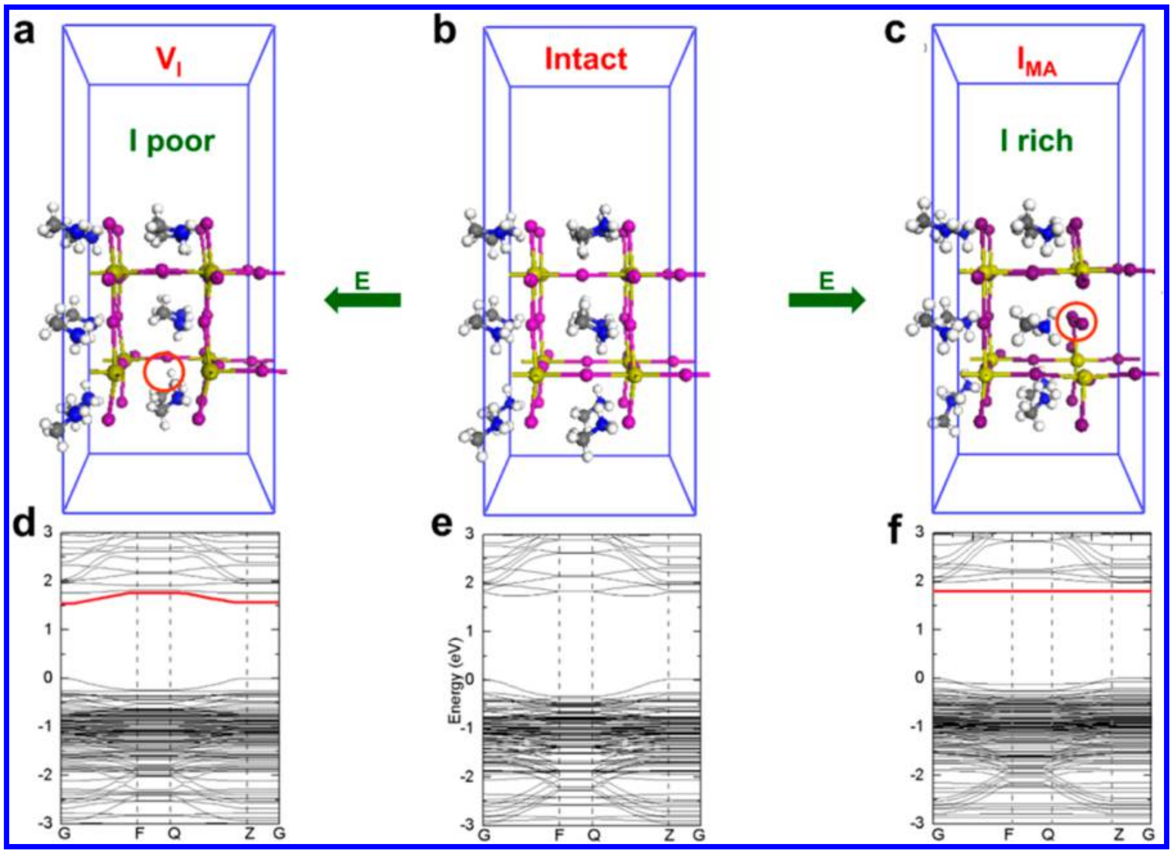

Figure 3. (a−c) Atomic structure of two-dimentional perovskite $(CH_3NH_3)_3Pb_2I_7$ viewed along the direction perpendicular to the *z*-axis. Color scheme: Pb: gold; I: purple; C: dark gray; N: blue; H: white. After adding an electric field, the I trimer can be induced in the I-poor region (a) and the Pb dimer can be induced in the I-rich region (c), compared to the initial crystal structure (b). Red circles in (a) and (c) represent the I trimer and Pb dimer, respectively. (d−f) Calculated band structure plot for intact (e), V_I^- (d), and I_{MA}^0 (f) along G(0,0,0) to F(0,1/2,0) to Q(0,1/2,1/2) to Z(0,0,1/2) to G(0,0,0). For defect V_I^-, there is an occupied defect state that lies below the perovskite CBM by 0.24 eV, which is shown by the red line. For I_{MA}^0, formation of an I trimer introduces an empty defect state close to (~0.35 eV) the bulk CBM, shown by the red line.

lateral device, these samples with a PMMA/PEG coating and in vacuum still present hysteresis and slow process (Figure S4). However, after PCBM treatment, the hysteresis has been significantly suppressed compared to the control sample (Figure 4a). Furthermore, only the PCBM coating sample shows a much faster response time (0.06 and 0.2 s) compared to the very slow voltage response time constant of around 2.5 and 8.5 s in the control sample (Figure 4b). The above results strongly suggest a stronger inhibiting effect of ion migration by PCBM. PCBM is not just a moisture-resistant layer but may have other effects to inhibit ionic motion. This result, in turn, suggests that the Galvanostatic characterization has higher sensitivity to evidence the inhibited ionic motion.

As we know, PCBM is normally used to suppress hysteresis in inverted structures[31−33] due to defect passivation and electron extraction. Although Sargent et al.[34] proposed that PCBM may also inhibit ion migration to suppress hysteresis, it still lacks evidence. With that in mind, compared with other coating layers, we speculate that PCBM can also strongly bond with perovskites, leading to inhibited ionic motion. We further use liquid-state ^1H NMR measurements to prove whether strong interaction exists between fullerenes and ions on the exposed surface of perovskites. The proton NMR spectra of four samples were compared (Figure4c): deuterated DMSO solution with PCBM (sample 1), with MAI (sample 2), with PCBM + MAI (sample 3), and PCBM + PbI_2 (sample 4). In the signals of sample 1, the methylene group close to the ester bond in PCBM is characterized by the peak at $\delta = 1.533$, and a visible chemical shift $\Delta\delta = 0.083$ of this peak is observed in samples 3 and 4 with PbI_2 and MAI, indicating interaction between iodine and PCBM. However, the proton resonance signal of $-NH_3^+$ in MAI presents a small shift from 7.522 to 7.531 ppm, indicating a very weak dipole interaction of MA^+ with the fullerene. For the interaction between the halogen and fullerene, the donor−acceptor nature due to charge transfer had previously been proven by Raman spectra, electron paramagnetic spectra (EPR), and absorption spectroscopy.[34−37] To directly confirm this strong interaction, here we devise a dissolution experiment for 3 mg mL^{-1} C_{60} with three solvents: methylbenzene (C_7H_8), iodobenzene (C_6H_5I), and chlorobenzene (C_6H_5Cl). When hydrogen in benzene is substituted for halogen (I/Cl), the C_{60} solubility correspondingly increases, which can be evidenced by a weakened Tyndall effect when a red laser beam passes through the solution, as shown in Figure 4d. This increased solubility should be independent of the polarity of the solvent due to the nonpolarity of C_{60}. To summarize, PCBM can interact with I^- in the perovskite film due to charge transfer to a buckyball and the van der Waals force with butyric acid methyl ester.

We close by demonstrating a new method of introducing PCBM into the perovskite film in n−i−p structure devices by immersing the as-prepared perovskite film in PCBM chlor-

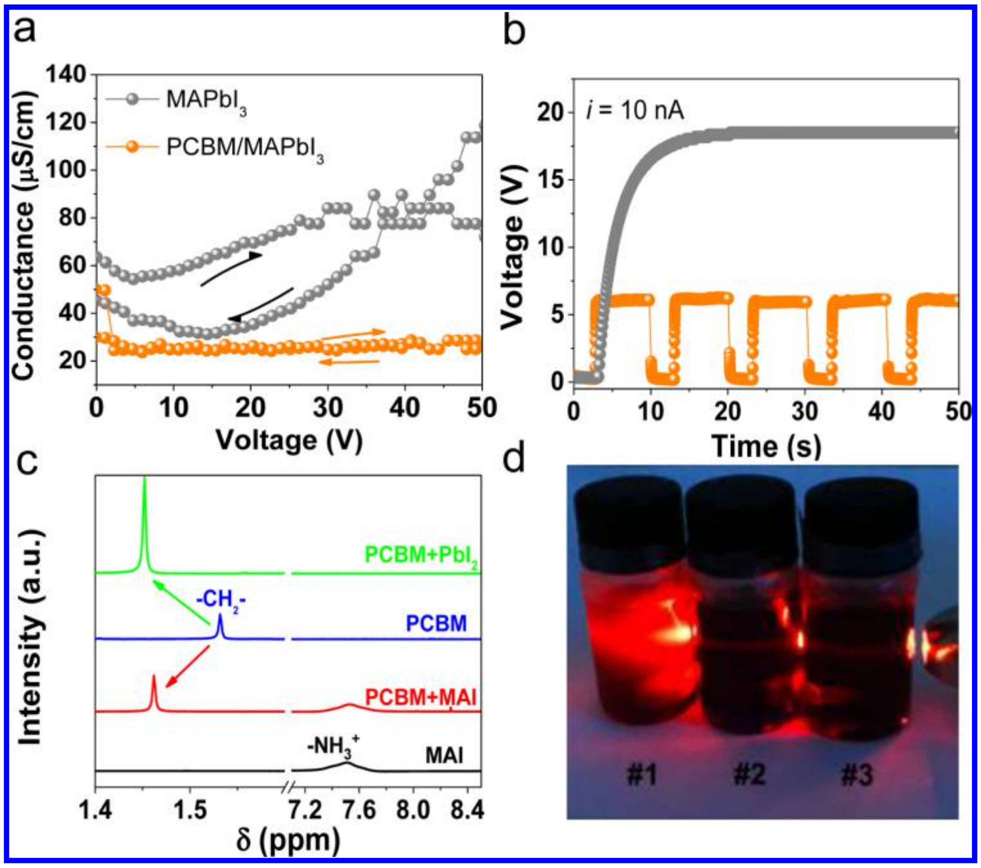

Figure 4. (a) Conductance of the perovskite film with and without PCBM treatment by PCBM spin-coating (2000 rpm/30 s) and annealing (105 °C/45 min) in a lateral structure device Au/MAPbI$_3$/Au with a 50 μm gap. (b) Voltage–time (V–t) characteristics for the perovskite film with and without PCBM treatment, under Galvanstatic measuring mode. (c) NMR for four samples, MAI (15 mg mL^{-1}), PCBM (saturated), MAI (15 mg mL^{-1}) + PCBM (saturated), and PbI$_2$(100 mg mL^{-1}) + PCBM (saturated), in deuterated dimethyl sulfoxide (DMSO). (d) Tyndall effect for C$_{60}$ (3 mg mL^{-1}) solution with different solvents (#1: methylbenzene; #2: iodobenzene; #3: cholorobenzene). A red laser passes through the solution from right to left.

obenzene solution (Figure 5a). Immersion time optimization is shown in Figure S5a. We perform the time-resolved photoluminescence (TRPL) test for three batches of samples: the control sample, the perovskite film after PCBM immersion, and the perovskite film after PCBM spin-coating. As presented in Figure 5b, PL spectra show a striking difference between spin-coated and immersed samples. The PCBM spin-coated sample shows corresponding lifetimes of 2.5 and 18.3 ns by using biexponential fitting, indicating a strong quenching effect. Very different from the spin-coated case, the PCBM-immersion sample shows a much longer minority carrier lifetime close to 101.5 ns by using single-exponential fitting, similar to the control sample. This result proves that PCBM will not cause the electron reflux here, and the improved hysteresis does not originate from an effective quenching effect by PCBM. Mass spectrometry (SIMS) measurements (Figure S6) reveal the PCBM distribution by this method, that PCBM penetrates into the film through grain boundaries and chemically absorb on the surface of the perovskite.

SEM characterization shows little difference in surface morphology after PCBM immersion (Figure S6). Current hysteresis is significantly decreased for the corresponding devices (Figure 5c). As a result, the PCBM-immersed sample demonstrates a higher steady-state efficiency of 15.6% than that (8%) of the control sample (Figure 5d). More importantly, the PSCs after PCBM immersion show a much better long-term stability in steady-state measurement mode, maintaining an approximately average 14% PCE for as long as ~2.3 × 10^5 s (64 h) of continuous output at MPP, compared to the quickly degraded PCE in control devices (Figure 5d).

Furthermore, after PCBM immersion, the perovskite film has a much faster response than that of the control sample in Galvanostatic measurements with ion blocking electrodes (Figure S7). On the basis of the above results plus the impedance spectra analysis (Figure S5), we speculate that the improved stability and suppressed hysteresis by PCBM immersion may originate from the inhibited ionic motion by PCBM. The influence of chlorobenzene is excluded because devices with 16 h immersion in the solvent without PCBM present no improvement in efficiency and hysteresis.

In summary, by introducing the integrated method to detect ion migration, a close relation has also been built up between ion migration and hysteresis in PSCs. We offer evidence on the posit that PCBM can inhibit ionic motion to suppress current hysteresis in PSCs by moisture resistance and donor–acceptor bonding. We close by demonstrating that hysteresis and stability can also be improved in the TiO$_2$ n–i–p structure if the PCBM molecule is chemicallyabsorbed on the exposed surface and grain boundaries of the perovskite film. Enlightened by these results above, we speculate that hysteresis can be eliminated if ion migration is minimized in PSCs.

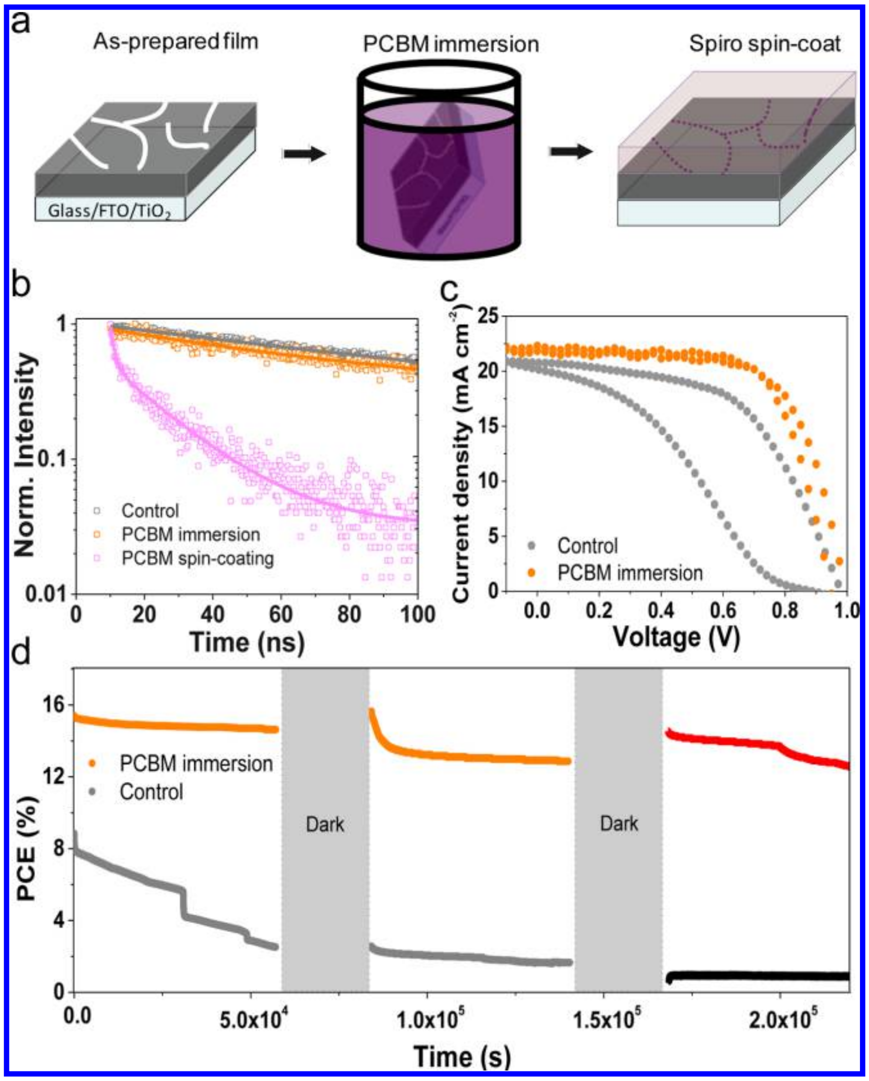

Figure 5. (a) Illustration diagram for the device preparation and PCBM immersion method. (b) TRPL characteristics for three batches of samples: control, with PCBM immersion treatment, and with PCBM spin-coating and annealing treatment. (c)Current–voltage (I–V) characteristics for devices with and without PCBM immersion treatment. (d) Steady-state efficiency at MPP as a function of time for devices with and without PCBM immersion treatment. Continuously working at a 0.7 V bias, the efficiency was recorded every 1 s. Devices went through 16 h of continuous work at MPP under AM1.5 illumination without any optical filter in the glovebox (humidity < 0.1 ppm) followed by 8 h of being stored in the dark for every 24 h.

■ ASSOCIATED CONTENT

Ⓢ Supporting Information

The Supporting Information is available free of charge on the ACS Publications website at DOI: 10.1021/acsenergylett.6b00060.

> Experimental methods and DFT calculation methods; PL spectra change at positive and negative poling after the current switches off; PL mapping of the peak position of the perovskite film before and after electric poling; optical image of the PMMA-coated sample in air and the control sample in vacuum; conductance and Galvanostatic measurements for the PMMA-coated perovskite film in air and the control sample in vacuum; PCBM immersion time optimization process; impedance spectra analysis; SEM characterization and SIMS measurements of the perovskite film before and after PCBM immersion; Galvanostatic measurements of PCBM-immersed and control samples (PDF)

■ AUTHOR INFORMATION

Corresponding Author

*E-mail: zhaoqing@pku.edu.cn.

Notes

The authors declare no competing financial interest.

■ ACKNOWLEDGMENTS

This work was supported by National 973 projects (2013CB932602, 2011CB707601, MOST) from the Ministry of Science and Technology, China and the National Natural Science Foundation of China (NSFC51272007, 61571015, 11234001, 91433102). Q.Z. acknowledges the Beijing Nova Program (XX2013003) and the Program for New Century Excellent Talents in University of China.

■ REFERENCES

(1) Burschka, J.; Pellet, N.; Moon, S.; Humphry-Baker, J. R.; Gao, P.; Nazeeruddin, M. K.; Gratzel, M. Sequential deposition as a route to

high-performance perovskite-sensitized solar cells. *Nature* **2013**, *499*, 316−319.

(2) Lee, M. M.; Teuscher, J.; Miyasaka, T.; Murakami, T. N.; Snaith, H. J. Efficient hybrid solar cells based on meso-superstructuredorganometalhalide perovskites. *Science* **2012**, *338*, 643−647.

(3) Liu, M. Z.; Johnston, M. B.; Snaith, H. J. Efficient planar heterojunction perovskite solar cells by vapour deposition. *Nature* **2013**, *501*, 395−398.

(4) Zhou, H. P.; Chen, Q.; Li, G.; Luo, S.; Song, T. B.; Duan, H.-S.; Hong, Z. R.; You, J. B.; Liu, Y. S.; Yang, Y. Interface engineering of highly efficient perovskite solar cells. *Science* **2014**, *345*, 542−546.

(5) Stranks, S. D.; Eperon, G. E.; Grancini, G.; Menelaou, C.; Alcocer, M. J. P.; Leijtens, T.; Herz, L. M.; Petrozza, A.; Snaith, H. J. Electron-hole diffusion lengths exceeding 1 micrometer in an organometaltrihalide perovskite absorber. *Science* **2013**, *342*, 341−344.

(6) Wei, J.; Zhao, Y. C.; Li, H.; Li, G. B.; Pan, J. L.; Xu, D. S.; Zhao, Q.; Yu, D. P. Hysteresis analysis based on the ferroelectric effect in hybrid perovskite solar cells. *J. Phys. Chem. Lett.* **2014**, *5*, 3937−3945.

(7) Frost, J. M.; Butler, K. T.; Brivio, F.; Hendon, C. H.; van Schilfgaarde, M.; Walsh, A. Atomistic origins of high-performance in hybrid halide perovskite solar cells. *Nano Lett.* **2014**, *14*, 2584−2590.

(8) Stranks, S. D.; Snaith, H. J. Metal-halide perovskites for photovoltaic and light-emitting devices. *Nat. Nanotechnol.* **2015**, *10*, 391−402.

(9) Snaith, H. J.; Abate, A.; Ball, J. M.; Eperon, G. E.; Leijtens, T.; Noel, N. K.; Stranks, S. D.; Wang, J. T.-W.; Wojciechowski, K.; Zhang, W. Anomalous hysteresis in perovskite solar cells. *J. Phys. Chem. Lett.* **2014**, *5*, 1511−1515.

(10) Grätzel, M. The light and shade of perovskite solar cells. *Nat. Mater.* **2014**, *13*, 838−842.

(11) Zhang, W.; Saliba, M.; Moore, D. T.; et al. Ultrasmooth organic−inorganic perovskite thin-film formation and crystallization for efficient planar heterojunction solar cells. *Nat. Commun.* **2015**, *6*, 6142.

(12) Zhang, W.; Pathak, S.; Sakai, N.; et al. Enhanced optoelectronic quality of perovskite thin films with hypophosphorous acid for planar heterojunction solar cells. *Nat. Commun.* **2015**, *6*, 10030.

(13) Ahn, N.; Son, D. Y.; Jang, I. H.; Kang, S. M.; Choi, M.; Park, N. G. Highly reproducible perovskite solar cells with average efficiency of 18.3% and best efficiency of 19.7% fabricated via Lewis base adduct of lead (II) iodide. *J. Am. Chem. Soc.* **2015**, *137*, 8696−8699.

(14) Jeon, N. J.; Noh, J. H.; Yang, W. S.; Kim, Y. C.; Ryu, S.; Seo, J.; Seok, S. I. Compositional engineering of perovskite materials for high-performance solar cells. *Nature* **2015**, *517*, 476−480.

(15) Wojciechowski, K.; Stranks, S. D.; Abate, A.; Sadoughi, G.; Sadhanala, A.; Kopidakis, N.; Rumbles, G.; Li, C. Z.; Friend, R. H.; Jen, A. K.; et al. Heterojunction modification for highly efficient organic−inorganic perovskite solar cells. *ACS Nano* **2014**, *8*, 12701−12709.

(16) Noel, N. K.; Abate, A.; Stranks, S. D.; Parrott, E. S.; Burlakov, V. M.; Goriely, A.; Snaith, H. J. Enhanced photoluminescence and solar cell performance via Lewis base passivation of organic−inorganic lead halide perovskites. *ACS Nano* **2014**, *8*, 9815−9821.

(17) Zhang, Y.; Liu, M.; Eperon, G. E.; Leijtens, T. C.; McMeekin, D.; Saliba, M.; Zhang, W.; et al. Charge selective contacts, mobile ions and anomalous hysteresis in organic−inorganic perovskite solar cells. *Mater. Horiz.* **2015**, *2*, 315.

(18) Eames, C.; Frost, J. M.; Barnes, P. R.F.; O'Regan, B. C.; Walsh, A.; Islam, M. S. Ionic transport in hybrid lead iodide perovskite solar cells. *Nat. Commun.* **2015**, *6*, 7497.

(19) Yang, T.-Y.; Gregori, G.; Pellet, N.; Grätzel, M.; Maier, J. The significance of ion conduction in a hybrid organic-inorganic lead-iodide-based perovskite photosensitizer. *Angew. Chem., Int. Ed.* **2015**, *54*, 7905−7910.

(20) Azpiroz, J. M.; Mosconi, E.; Bisquert, J.; De Angelis, F. Defect migration in methylammonium lead iodide and its role in perovskite solar cell operation. *Energy Environ. Sci.* **2015**, *8*, 2118−2127.

(21) Xiao, Z.; Yuan, Y.; Shao, Y.; Wang, Q.; Dong, Q.; Bi, C.; Sharma, P.; Gruverman, A.; Huang, J. S. Giant switchable photovoltaic effect in organometaltrihalide perovskite devices. *Nat. Mater.* **2014**, *14*, 193−198.

(22) Yuan, Y.; Wang, Q.; Shao, Y.; et al. Electric-field-driven reversible conversion between methylammoniumlead triiodide perovskites and lead iodide at elevated temperatures. *Adv. Energy Mater.* **2016**, *5*, 1500615.

(23) Leijtens, T.; Hoke, E. T.; Grancini, G.; Slotcavage, D. J.; Eperon, G. E.; Ball, J. M.; De Bastiani, M.; Bowring, A. R.; Martino, N.; Wojciechowski, K.; et al. Mapping electric field-induced switchable poling and structural degradation in hybrid lead halide perovskite thin films. *Adv. Energy Mater.* **2015**, *5*, 1500962.

(24) Leijtens, T.; Srimath Kandada, A. R.; Kandada, R.; Eperon, G. E.; Grancini, G.; D'Innocenzo, V.; Ball, J. M.; Stranks, S. D.; Snaith, H. J.; Petrozza, A. Modulating the electron-hole interaction in a hybrid lead halide perovskite with an electric field. *J. Am. Chem. Soc.* **2015**, *137*, 15451−15459.

(25) Kuokstis, E.; Yang, J. W.; Simin, G.; Khan, M. A.; Gaska, R.; Shur, M. S. Two mechanisms of blueshift of edge emission in InGaN-based epilayers and multiple quantum wells. *Appl. Phys. Lett.* **2002**, *80*, 977.

(26) Eliseev, P. G.; Perlin, P.; Lee, J.; Osiński, M. Blue temperature-induced shift and band-tail emission in InGaN-based light sources. *Appl. Phys. Lett.* **1997**, *71*, 569.

(27) Yokota, I. On the electrical conductivity of cuprous sulfide: adiffusion theory. *J. Phys. Soc. Jpn.* **1953**, *8*, 595−602.

(28) Yokota, I. On the theory of mixed conduction with special reference to conduction in silver sulfide group semiconductors. *J. Phys. Soc. Jpn.* **1961**, *16*, 2213−2223.

(29) Baiatu, T.; Waser, R.; Hardtl, K. H. Electrical degradation of perovskite-type titanates: III, Amodel of the mechanism. *J. Am. Ceram. Soc.* **1990**, *73*, 1663−1673.

(30) Agiorgousis, M. L.; Sun, Y. Y.; Zeng, H.; Zhang, S. B. Strong covalency-induced recombination centers in perovskite solar cell material $CH_3NH_3PbI_3$. *J. Am. Chem. Soc.* **2014**, *136*, 14570−14575.

(31) Shao, Y.; Xiao, Z.; Bi, C.; Yuan, Y.; Huang, J. S. Origin and elimination of photocurrent hysteresis by fullerene passivation in $CH_3NH_3PbI_3$ planar heterojunction solar cells. *Nat. Commun.* **2014**, *5*, 5784.

(32) Xiao, Z.; Bi, C.; Shao, Y.; Dong, Q.; Wang, Q.; Yuan, Y.; Wang, C.; Gao, Y.; Huang, J. S. Efficient, high yield perovskite photovoltaic devices grown by interdiffusion of solution-processed precursor stacking layers. *Energy Environ. Sci.* **2014**, *7*, 2619−2623.

(33) Tress, W.; Marinova, N.; Moehl, T.; Zakeeruddin, S. M.; Nazeeruddin, M. K.; Gratzel, M. Understanding the rate-dependent J-V hysteresis, slow time component, and aging in $CH_3NH_3PbI_3$ perovskite solar cells: the role of a compensated electric field. *Energy Environ. Sci.* **2015**, *8*, 995−1004.

(34) Xu, J. X.; Buin, A.; Ip, A. H.; Li, W.; Voznyy, O.; Comin, R.; Yuan, M. J.; Jeon, S. M.; Ning, Z. J.; McDowell, J. J.; et al. Perovskite-fullerene hybrid materials suppress hysteresis in planar diodes. *Nat. Commun.* **2015**, *6*, 7081.

(35) Li, C.; Chueh, C.; Ding, F.; Yip, H.; Liang, P.; Li, X.; Jen, A. K.Y. Doping of Fullerenes via anion-induced electron transfer and its implication for surfactant facilitated high performance polymer solar cells. *Adv. Mater.* **2013**, *25*, 4425−4430.

(36) Limonov, M. F.; et al. Phonons and electron-phonon interaction in halogen-fullerene compounds. *Phys. Rev. B: Condens. Matter Mater. Phys.* **1998**, *57*, 7586594−7.

(37) Burtsev, A. V.; Kemnitz, E.; Troyanov, S. I. Synthesis and structure of fullerene halides $C_{70}X_{10}$ (X= Br, Cl) and $C_{78}Cl_{18}$. *Crystallogr. Rep.* **2008**, *53*, 639−644.